High resolution K_S polarization mapping of OH 231.8+4.2 (OH 0739-14) with SOFI

N. Ageorges[1,2] **and J.R. Walsh**[2]

[1] Physics Department, National University of Ireland – Galway, Galway, Ireland (nageorge@eso.org)
[2] European Southern Observatory, Karl-Schwarzschild Strasse 2, 85748 Garching bei München, Germany (jwalsh@eso.org)

Abstract. The bipolar reflection nebula OH 231.8+4.2 (OH 0739-14) centred on the Mira variable star QX Pup has been mapped at K_S in linear polarization using the ESO SOFI near-infrared multi-mode instrument. The large scale linear polarization features agree with previous studies, validating the polarimetric mode of the instrument. However the high spatial resolution of the polarization map reveals considerable structure, some of which finds correspondence in the surface brightness images. The core is crossed by low polarization filaments; the northern lobe reveals an axial finger and a rim of very high linear polarization (upto 80%) whilst the southern lobe shows less polarization contrast. There is a trend in polarization perpendicular to the bipolar axis in both lobes. The individual linear polarization features most probably arise from localised dust structures with distinct orientations leading to differing polarization through single scattering. A single scattering geometric model, consisting of two lobes of ellipsoidal section and a central dense disk, is considered which can explain the general features of the intensity and polarization images.

Key words: ISM: reflection nebulae – ISM: individual objects: OH 0739-14, OH 231.8+4.2 – techniques: polarimetric – stars: individual: Qx Pup

1. Introduction

The bipolar nebula OH 231.8+4.2 (IRAS OH 0739-14, sometimes called the Calabash nebula) is centred on the Mira variable QX Pup and is a source of line and continuum emission at many wavelengths. It displays strong extended optical and IR structure about $40''$ in length, which is very highly polarized (Scarrott et al. 1990 for the optical; Kobayashi et al. 1978; Heckert & Zeilik 1983; Shure et al. 1995; Kastner & Weintraub 1995 for the IR). At the extremity of the southern bipolar lobe, there are high velocity emission line knots, similar to Herbig-Haro objects (Reipurth 1987). The central variable star has an

amplitude of $\sim$2 mag., a period of $\sim$700 days (Kastner et al. 1992) and a spectral type of M9 III (Cohen 1981; Cohen et al. 1985). The star is not directly visible in the optical on account of a waist of high extinction, but dominates the structure at longer wavelengths (Woodward et al. 1989). Kastner et al. (1992) have resolved the star from the surrounding nebula at K and L and deduce that it is a typical Mira variable. The object was first discovered on account of its OH maser emission (Turner 1971) and mm wave CO mapping has shown a high velocity outflow oriented at $\sim$40° to the plane of the sky with deprojected velocities upto $330 \, \mathrm{km \, s^{-1}}$ for the southern lobe and $90 \, \mathrm{km \, s^{-1}}$ for the northern lobe (Alcolea et al. 1996). It is generally considered to be a transition object between the Asymptotic Giant Branch (AGB) and the Planetary Nebula phases in which the high velocity stellar wind is blowing out the AGB dust envelope. The estimated mass of the molecular and dust envelope is estimated to be $\sim$0.5 - 1$M_\odot$, consistent with a main sequence mass $\sim$3 $M_\odot$ (Kastner et al. 1998).

Aside from its great astrophysical interest as a short-lived proto-planetary nebula, OH 231.8+4.2 is a useful test source for polarization measurements. From the optical to the L band it possesses high linear polarization (upto 50% in large apertures, Shure et al. 1995) and so is a useful polarization calibrator. It cannot be stated with any certainty that it possesses the most important attribute for a calibrator - that the polarization is non-variable, but the high polarization makes it useful as a calibrator for the polarimetric efficiency and for position angle determination. In addition, since the polarization pattern is centro-symmetric along the bright lobes (although not in the equatorial direction) and extended over a length of about $50''$, it provides an ideal source to confirm any instrumental depolarization effects. In consequence OH 231.8+4.2 was selected as a test source for the commissioning of the SOFI polarimetric mode. The quality of the instrument and the observations proved to be excellent and yielded the highest resolution near-IR polarization map of this source.

The instrumental set-up and the observations are detailed in Sect. 2 and the polarization results presented in Sect. 3. The spatial polarization structure is discussed in Sect. 4 together with conclusions about the geometry of the elongated dust cloud and the scattering properties of the grains.

2. Observations

2.1. SOFI

SOFI (Son OF Isaac, Moorwood et al. 1998) is an infrared spectrograph and imaging camera installed at the ESO 3.5m NTT. It has a focal reducing camera and is capable of performing near-infrared imaging, spectroscopy with grisms and polarimetry. Imaging can be achieved with 3 different plate scales (0.144, 0.276 and 0.292″ per pixel) using broad and narrow band filters in the wavelength range 0.9 to 2.5 μm. The detector is an Hawaii HgCdTe 1024×1024 pixels array, with a quantum efficiency of 65% (Moorwood et al. 1998). Imaging polarimetry is possible over the near-IR range using a Wollaston prism installed in the grism wheel and a special mask in the aperture wheel. The mask has three focal plane apertures with separation chosen so that the image pairs resulting from the Wollaston do not overlap on the detector. Broad and narrow filters may be selected together with the Wollaston. Using the Wollaston and aperture mask three pairs of images are collected; one pair for the object and two pairs for offset sky. The Wollaston outputs two divergent beams with the E-vector oriented parallel and perpendicular to its axis; the difference between the two images allows one Stokes parameter to be determined. The size of each strip is about 1023 by 145 pixels, separated by about 8 pixels.

2.2. Observational set-up

The observations of OH 231.8+4.2 were performed on 1997 August 8 using the 0.292″ pixel scale. Data have been acquired with a narrow band filter of 2.162 μm central wavelength and 0.275 μm width (K_S) using double correlated sampling with 60 samples. Double correlated reading measures the signal as the difference between the reset voltage of a diode and the post exposure voltage; the noise from thermal capacitance changes are eliminated as a result. For each of two position angles of the Wollaston, separated by 45° measurements were repeated three times with an exposure time of 70.9s. Between each acquisition the position of the nebula on the chip was displaced, to avoid using exactly the same detector position. This also has the advantage that no extra sky data needed to be acquired. By subtracting one data set from the other, the sky contribution can be removed. The sets of three images allowed one of the Stokes parameters, U or Q, to be measured; the set taken at a position angle rotated by 45° allowed the other Stokes parameter to be determined.

3. Reductions and results

3.1. Data reduction

The six regions on the detector, one for the object (O) and two for the sky (S_1, S_2), each of them with two transmissions of the Wollaston (referred to as O (ordinary ray) and E (extraordinary ray)), at which data have been acquired, are called hereafter On^o,On^e, Sn_1^o,Sn_1^e and Sn_2^o,Sn_2^e, where n refers to the repeat observations taken with the object shifted on the detector. There are two ways in which this data can be treated: either the mean sky can be formed from the offset sky images from (Sn_1^o, Sn_2^o) and (Sn_1^e, Sn_2^e) and subtracted from the corresponding On^o and On^e; or the repeat ('nodded') observations on the object images can be subtracted (i.e. $O1^o$ and $O2^o$), for the same Wollaston transmission. The latter procedure has the advantage that the sky is subtracted from the same detector pixels as the object and the procedure should be insensitive to pixel-to-pixel variations; however it has the potential disadvantage that for extended objects there may be stars in the same position as the object in shifted frames. Comparison with the result using the mean sky formed from the offset images can be used to ensure that no stars are in fact subtracted from the nebular image. The nodding procedure was followed to form the nebular images before combination, with the modification that the image to be subtracted was formed from the mean of the other two (i.e. $O1^o$ minus mean of $O2^o$ and $O3^o$). Thus a total of 12 object images were processed (three positions of the object on the array, each with O and E and with the instrument rotated by 45°). Flat field exposures were taken using dome illumination with the same filter and Wollaston prism. Flat field images were created after extraction of similarly defined areas (same size and position) from the original dome flat fields and normalization. It was found that the flat fields implied small ($\lesssim$5%) but significant changes in the pixel-to-pixel response.

The basic data reduction steps were performed with the 'eclipse' package (Devillard 1997). The source frames were first sky subtracted, flat fielded and then bad pixel corrected. Sky data, determined as explained above, has been used to derive bad pixels maps, via a 'median threshold' method which detects the presence of spikes above or below the local mean in the individual image. Assuming the signal is smooth enough, bad pixels are found by computing the difference between the image and its median filtered version, and thresholding it. The algorithm used to clean out a frame from bad pixels replaces bad pixels by an average of the valid pixels from the 8 closest neighbours.

Combining the object images from one set of O and E ray Wollaston data allows one Stokes parameter to be derived. One of the data sets must be rotated by 45° in order to determine the linear polarization from two Stokes parameters. To avoid any artefact that the rotation algorithm might create in the structure of the data, it was decided to rotate the images acquired with the Wollaston at 0° by +22.5° and the ones with a position angle rotated by 45° by -22.5° respectively, so that both data sets are equally affected by this operation. The final results were compared with those produced by rotating one set by 45°; no significant differences were noted but the more conservative procedure was followed.

To estimate the spatial variation of the polarization, the Q and U Stokes parameter images had to be shifted to the same position. For this purpose, the centroid position of the star at position $\Delta X = +16''$ and $\Delta Y = +9''$ from the core of OH 231.8+4.2 (Fig. 1) was calculated to within a tenth of a pixel, and used to determine the necessary image shift. The IRAF 'imshift' procedure was used, ensuring that all images are at the same position
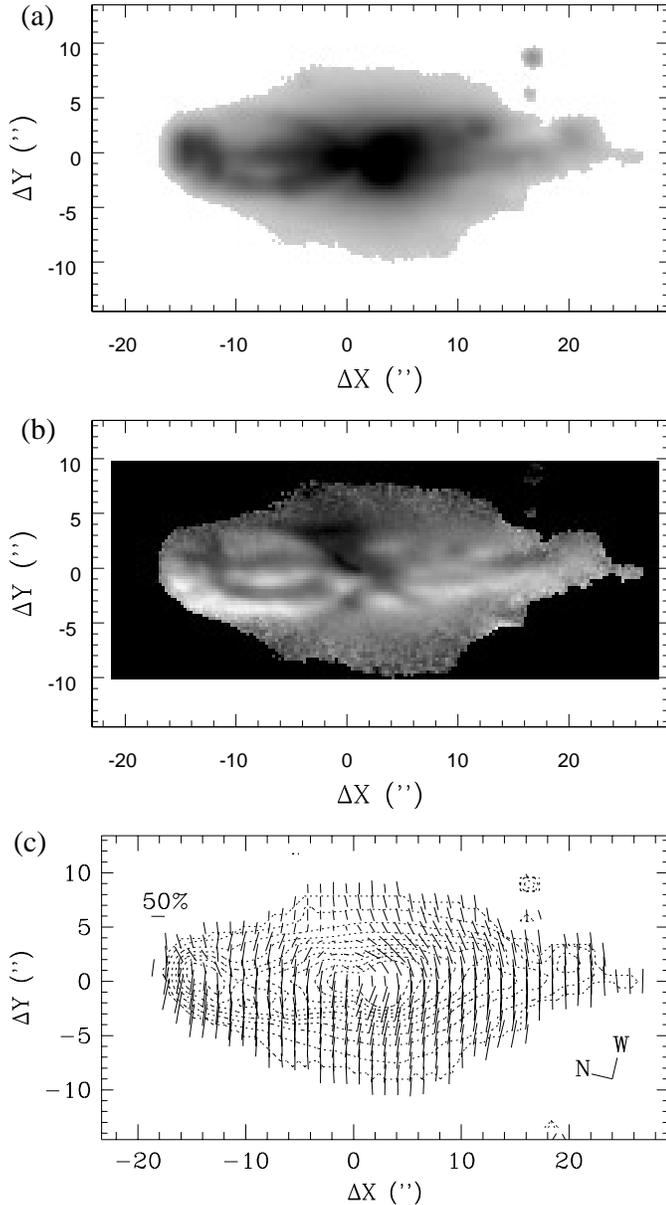
Fig. 1. a K_S total (relative) intensity map of OH 231.8+4.2 is displayed in a logarithmic plot. The data are at the original pixel size (0.292″); **b** greyscale plot of the degree of linear polarization map of OH 231.8+4.2 is shown, with a range from 0 (black) to 90% (white); **c** polarization vector map of OH 231.8+4.2 derived from the K_S images is shown. Logarithmic contours of the intensity map are overplotted (dashed lines). The vectors have been binned 2×2 pixels before plotting and only every 2nd vector is plotted for clarity

within two tenths of a pixel. Since, however, combining images with a rotation of 45° is the worst case situation as far as sampling is concerned, the images were first pixel replicated to 4×4 smaller pixels. Then the images were aligned using this star and rotated to a common position angle. The final images were then 4×4 binned back to the original pixel scale. A seeing of 1.0″ (3.5 pixels) was measured during the observations, although the data taken at a PA of 45° had slightly worse seeing. After the

rotation, alignment and summing of the three data sets acquired with one given polarization (O or E ray for the Wollaston at 0 or 45°), the degradation of FWHM was found to be minimal (less than 0.1″).

Polarization maps have been created both for flat-fielded and non flat-fielded data using the imaging polarimetry package IRAF.stecf.impol. The SOFI detector is known to suffer from a signal dependent bias so that the absolute level of the flat field exposure can induce artefacts into the flat field. The flat fields were fairly flat in signal over the exposed regions of the chip (rms ≤5%), so the induced effects should not be large. The primary aim of the flat fielding was to reduce pixel-to-pixel scatter. Examination of the final images showed that the flat-fielded images were indeed slightly smoother than the non flat-fielded ones. Comparing the flat-fielded and non flat-fielded polarization maps showed that there were no features, above the noise, detected in one image which were not present in the other.

The instrumental polarization had not yet been determined prior to the observations of OH 231.8+4.2. A series of observations of the unpolarized standard star HD 94851 (B polarization 0.057%, Turnshek et al. 1990) were made rotating the instrument by 22.5 degrees from 0 to 180° in steps of 22.5°. All the O and E ray data at all position angles were reduced together for both flat fielded and non-flat fielded data frames. The results were obtained fitting a cosine $2\times\theta$ curve to all the data points using least squares. For the flat fielded data the instrumental polarization at K_S was found to be 1.03±0.07% at 142.2±1.8°. This determination assumes that the polarization of HD 94851 at 2.1 μm is zero; the value is not known but is probably less than 0.01% assuming a normal interstellar polarization curve. This value of the instrumental polarization was used to correct the linear polarization and position angle of the OH 231.8+4.2 data.

3.2. Results

The total intensity K_S map formed by summing all the images in the two Wollaston sub-images and two orientations, aligned, as described above, on the star to the south-west, is shown in Fig. 1a in a logarithmic plot. Part of the extended nebulosity to the S, containing Herbig-Haro objects (Reipurth 1987) was out of the imaged area. The sky subtracted and flat fielded images in the two Wollaston sub-images and at the two rotator angles were combined to form images and errors in Q and U Stokes parameters using the IRAF.stecf.impol package. The errors were propagated from the original images assuming a conversion of 5.9 e$^-$ per ADU and a read-out noise of 12 e$^-$ per pixel. The linear polarization, the corresponding error map, the position angle and error image were determined. The polarization was corrected for non-negativity bias (e.g. Wardle & Kronberg 1974) and the position angle errors determined from the distribution given by Naghizadeh-Khouei & Clarke (1993). No correction was applied for intervening interstellar polarization. Fig. 1b shows the image of the linear polarization in OH 231.8+4.2 in an unbinned form (cut-off in polarization error is 10%). Fig. 1c shows the 2×2 pixel binned linear polarization map. The cut-off in polar-

ization error is 10% in this map. A wealth of structure in the polarization map is evident attesting to the fact that it is not a simple centro-symmetric reflection nebula. The polarization structure is discussed in Sect. 4.

In order to compare the SOFI polarimetry with previous work, the signal in a number of apertures was summed and the polarization and position angle values determined. Measurements were made in three circular apertures at the centre, at 2.5″E,7.0″N and at 2.5″W,7.0″S (respectively the apertures C, A and E of Shure et al. 1995) and are listed in Table 1. Fig. 2 shows a sketch of the appearance of the nebula in K_S with the positions of these three apertures shown by dotted circles. In addition the linear polarization at six other positions of interest, whose exact positions are detailed in Table 1, was determined for the northern crescent knot, the fainter central knot, the whole of the brighter S knot, the peak of the southern knot, the knot to the south-west and the extreme southern knot. Aperture diameters, selected to include these features, are listed in Table 1 and the aperture positions are also shown in Fig. 2. The linear polarization and position angle values at K from Shure et al. (1995) are also listed in the last column of Table 1. The agreement is generally excellent: for position C the linear polarization and position angle agree within errors; for position A (the brightest region) the agreement in polarization is fair; for position E, the error bars are larger since this is the faintest region of the three, and the position angle is discrepant. The small discrepancies may be partly attributable to differences in the exact positioning of the different apertures. The last item in Table 1 is the alignment star to the SE (upper right in the figures); it has a polarization consistent with zero to within the errors.

Given this good agreement between the aperture polarimetry results presented in Table 1 and those of other observers, the results of the imaging polarimetry with SOFI are considered to be reliable, although a full calibration of the instrument has not yet been performed. It is concluded that there is no large correction for polarizing efficiency or position angle to be applied. Although this source is certainly useful as a high polarization calibrator, the position and size of the aperture must be carefully chosen otherwise discrepant results can be obtained.

Fig. 3 shows the profiles of total intensity, linear polarization and position angle along the long axis of the nebula (PA 20°); each point corresponds to three pixels binned. Offset 0 corresponds to the position of the central star as estimated by comparison with the images of Kastner et al. (1998). This central position also displays the lowest value of linear polarization and the position angle shows an abrupt change across this region. Error bars are shown for the polarization and position angle in Fig. 3.

4. Discussion

4.1. Intensity and polarization morphology

The K_S total intensity morphology shown in Fig. 1a consists of two lobes which however are substantially different in appearance. The sketch of the nebula in Fig. 2 indicates the morphological features distinguished here. The northern lobe, which is
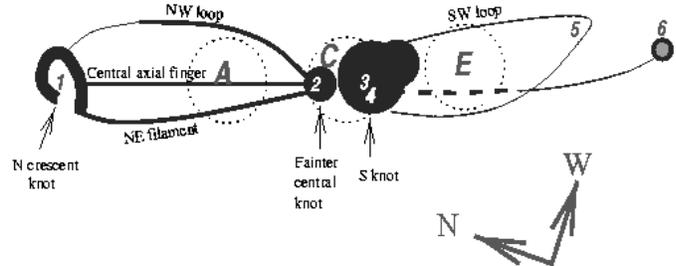
Fig. 2. A sketch of the appearance of OH 231.8+4.2 at K_S is shown with the features referred to in the text labelled. Apertures A, C and E (Shure et al. 1995) are indicated by dashed circles and the centres of six other apertures at which the linear polarization was determined (Table 1) are numbered
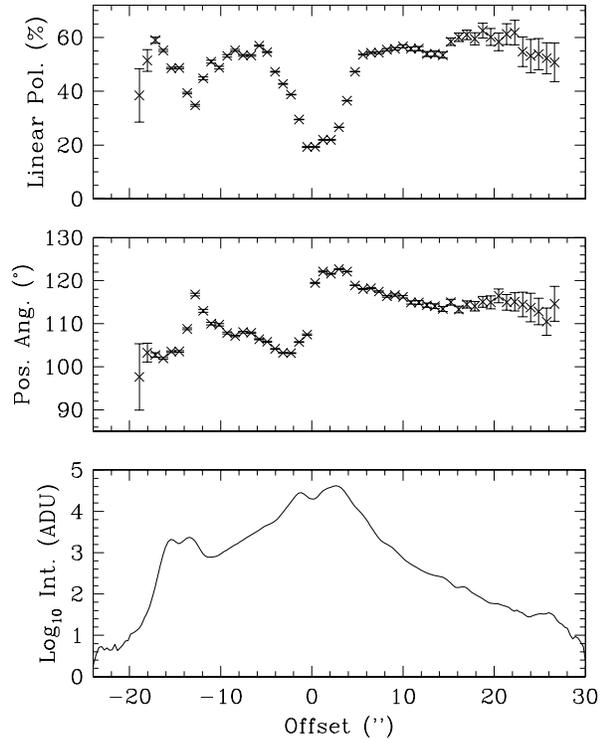
Fig. 3. 3×3 pixels binned cuts through the long axis of the nebula at absolute PA of 20° (i.e. the horizontal in Figs. 1a-c) are illustrated. The top plot shows the linear polarization, the middle plot the polarization position angle and the bottom plot the log of the (relative) total signal (Stokes I). Offset 0 corresponds to the position of the central Mira star

tilted towards the observer (from the plane of the sky) by about 40° (e.g. Cohen et al. 1985; Kastner et al. 1992; Scarrott et al. 1990) has a central finger and two curling lobes emerging from the core which hides the Mira star QX Pup behind a dense disc of dust (Kastner et al. 1998). The finger and north-eastern filament meet in the northern crescent shaped knot (#1 in Table 1). The southern lobe is less sharply defined; the eastern loop is not present and the western one is composed of several knots. The high resolution achieved without adaptive optics can be appreciated by comparison with the K band AO imaging of Kastner et al. (1998). The features on the AO image are not much sharper

Table 1. Aperture polarimetry of OH 231.8+4.2

Aperture Name	Offset[†] ($''$)	Aperture Diam ($''$)	Linear Poln. (%)	Poln. PA ($°$)	Literature[*] Poln (%)	PA ($°$)
C	0.0,0.0	4.0	23.44±0.03	108.69±0.03	24.4±0.5	110
A	+2.5,+7.0	4.0	50.84±0.08	108.32±0.05	50.0±0.7	112
E	−2.5,−7.0	4.0	46.15±0.06	124.54±0.04	49.8±2.4	117
#1	+5.0,+13.8	3.5	39.59±0.10	108.40±0.07		
#2	+0.7,+1.7	2.3	38.90±0.04	104.95±0.03		
#3	−0.8,−2.1	4.1	25.48±0.02	109.74±0.02		
#4	−0.3,−2.1	1.8	29.33±0.04	101.31±0.04		
#5	−4.1,−10.2	2.3	48.57±0.21	126.08±0.12		
#6	−7.5,−18.5	2.9	50.51±0.74	116.93±0.42		
Star X		2.9	2.65±2.63	179.84±31.9		

[†] Offsets in RA and DEC, relative to the the position of the central star: East +, South −
[*] Literature values from Shure et al. (1995) in K band.

than in Fig. 1a and the lobes are not strikingly composed of many resolved knots.

Kastner et al. (1992) have also published a K band polarization map (their Fig. 2). There is broad agreement with their Fig. 2 but the SOFI map has higher spatial resolution and signal-to-noise. The linear polarization images in Figs. 1b and c show important features in common with the total intensity map which bring a wealth of new information on the structure of the nebula and the nature of the dust features. The new polarization features can be summarized as follows:
the central finger in the N lobe has a higher polarization than the immediate surroundings, by about 20% (Figs. 1b and c);
the northern knot has low polarization (offset -13$''$ in Fig. 1b and c) and the position angle is distinct across the knot;
there is a line of lower polarization running diagonally across the central region (Figs. 1b and c);
there is an outer halo of lower polarization (though still ∼30%) around the nebula (Figs. 1b and 1c);
the polarization increases from west to east across both lobes, but most noticeably for the northern lobe (Fig. 1b,c).
Comparing Figs. 1a and 1b it is clear that the finger and loops visible in total intensity in the N lobe are also more strongly polarized, whilst in the southern lobe (tilted by ∼40° away from the plane of the sky) there is no such clear 1:1 correspondence.

The most remarkable features are the elongated very high polarization features in the north lobe. Along the central finger the polarization increases from 48 to 71% (at 5.3$''$ from the central star) before declining again to values around the average for the N lobe (40%). The eastern filament in the N lobe has its peak value of 80% at an offset of 10.5$''$ from the centre; the position angle of this entire feature is 20–30° greater than the surroundings. The other dominant feature in this lobe, the knot at -15$''$ offset, however has low (30%) polarization and the position angle is distinct and close to the value for the S lobe. This difference may be due to intrinsic emission diluting the polarization or, more probably, an orientation closer to that of the S lobe (i.e. in the background). The south lobe has a feature along its length with linear polarization decreasing from 70% to 60% although the collimation of this feature is much less clear

than for the N lobe and there is no distinction in position angle relative to the surrounding lobe. This high polarization feature in the S lobe is towards the eastern side and is more similar to the high polarization eastern edge to the N lobe, but does not correspond clearly to a filamentary feature on the intensity image. The lower contrast of features in the S lobe may be caused by obscuration by the equatorial disc. The knot at +11$''$ offset on the western side of the S lobe with 35–40% polarization parallels the low polarization crescent knot in the N lobe but is less striking in its brightness and polarization minimum.

The almost circular cloud of lower polarization values surrounding the bipolar nebula are interpreted as belonging to the disc. The low polarization on the front side of this disc is clearly seen as the minimum a few arsec to the south of the position of the central star in Figs. 3 and 1b and c. Note also how the position angle of polarization changes across this region (Fig. 3 offsets 0 to +8$''$). This coincides with the brightest spot in Fig. 1a. If this was single scattering from the surface of the disc, the polarization would be expected to be higher than for the northern lobe at a similar offset. Since this region is offset from the position of the central star, the scattered flux cannot be diluted by direct radiation, so that multiple scattering must be occurring. The minima in polarization around the central star can be attributed either to viewing directly along the flaring edge of the bipolar lobe as it emerges from the thick disk, or to multiple scattering at the dense interface region between the equatorial disc and one of the bipolar cavities. The gradual increase in polarization along the bipolar axis into the south lobe (Fig. 3) can be explained by an increasing mix of scattered flux from the bipolar lobe over that of the disc as the line of sight optical depth through the disc decreases outward.

The lower polarization region around the nebula that shows the bulk of the polarization vectors are aligned radially, rather than normal to the direction to the central star, as first noted by Dougados et al. (1991). This has been traditionally ascribed to multiple scattering in an optically thick dusty disc (e.g. Kastner & Weintraub 1995; see also Bastien & Ménard 1990). The possibility that there is substantial flux scattered off the lobes reflected from the surface of the disc seems less likely; the scat-

tering geometry would produce a range of position angles with only two scatterings and so is probably not a significant effect. However the constancy of the position angle over large areas of the disc, in particular to the east (Fig. 3), suggest a large scale organization of grain alignment. The degree of multiple scattering is primarily dependent on the optical depth, which should vary with position around the disc, so may not be able to produce such a coherent pattern of polarization vectors. Bulk alignment of (non-spherical) grains by a frozen-in magnetic field might however be capable of explaining the observed configuration (e.g. Hildebrand 1983).

4.2. Dust features

The high polarization, together with the stronger K_S signal, over the finger and the eastern loops in the northern and southern lobes requires to be explained. The higher K_S flux must be attributable to high column depth of dust since it cannot be explained together with increased polarization: polarization increases while scattered flux decreases with increasing scattering angle for interstellar dust scattering situations (e.g. Mathis 1990). Two possibilities are considered for the high polarization features:

– the high polarization is caused by differing scattering angles. The higher values correspond to values closer to 90° scattering where polarization, at least for Rayleigh scattering, is maximum. Since the N lobe is tilted towards the observer it would imply that the finger and the eastern wall are tilted more away from the observer. To avoid the over-complex view that the lobe is composed of several components, all with different tilts, the lower polarization regions could represent an integration along the line of sight of a range of scattering angles. The lower polarization of the western edge then indicates a smaller scattering angle and hence an east-west tilt of a lobe of elliptical section. The central finger would have to be at a rather different tilt from the lobe axis for its polarization to be dissimilar to the surroundings;
– the dust in these features is indeed different from that in the bulk of the lobe. In order for the polarization to be higher then the particles would have to be smaller. If the lobes are hollow then it is difficult to see why one edge of the lobe should happen to have differing particles to those averaged through the lobe. The hypothesis of differing particles can only realistically be applied to the finger.

The first suggestion could explain the differing polarization of the loops, as compared to the material within the lobe, by having the lobe more elongated in the line of sight. The tilt in polarization perpendicular to the projected major axis of the nebula could be explained by an elliptical section with the eastern side more twisted away from the observer. Fig. 4 shows a sketch of this configuration. A 3-D dust nebula with this shape was generated and scattered intensity and polarization maps were computed (cf. the polarization models for η Carinae in Meaburn et al. 1993). Rayleigh scattering was employed, although problems with the presence of small grains have been
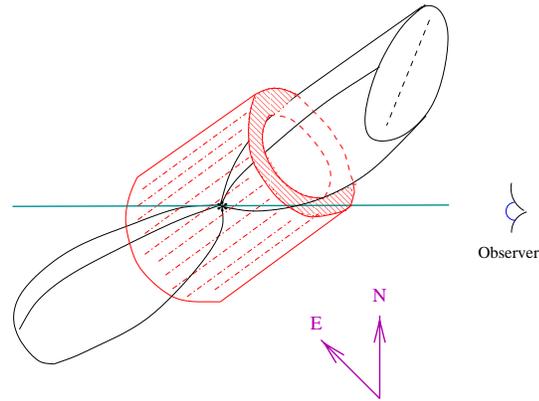

Fig. 4. 3D representation of OH 231.8+4.2 nebula and its orientation towards the observer showing the rotated spheroidal shell geometry of the lobes explained in the text
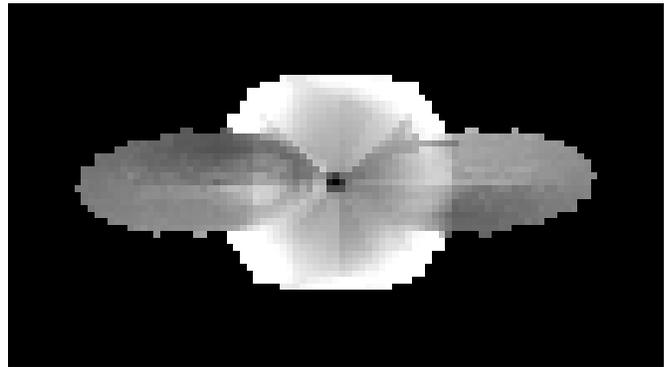

Fig. 5. Linear polarization map of the 3-D model nebula consisting of a pair of triaxial ellipsoidal shells whose major axes almost intersect at the central illuminating source and an equatorial disc whose thickness along the bipolar axis is 40% of the length of each lobe. The structure is tilted at 40° to the plane of the sky and the bipolar axis is rotated by 40° around the nebula major axis

suggested by Shure et al. (1995) on account of the similar optical depth with wavelength in the near-IR. It was found from the scattering model that the twisted ellipsoidal geometry produces a reverse (i.e. increasing east-west) trend in the polarization across the south lobe. Thus there is a suggestion that the southern lobe is twisted in the opposite sense about the long axis to the northern lobe. However given the irregularity of the southern lobe this is no more than a suggestion. A polarization map formed from the 3-D model is shown in Fig. 5 where the nebula was tilted at 40° to the plane of the sky and the lobes of elliptical section were twisted about their major axis by 40°. A qualitative match to the fall-off of intensity along the axis (c.f. Fig. 3) is achieved for a density gradient of $r^{-0.5}$ along the lobes. A small central disc, whose thickness is however 40% of the length of each lobe, and has a density gradient $\propto r^{-2}$ has been included. The model manages to reproduce a number of the large scale features such as the bright loops bounding the lobes, as well as several salient features such as the low polarization filament to the west of the centre and the east-west slope in polarization

across the N lobe. The slope in polarization of the S lobe is in the reverse direction to that observed and the lower polarization and radially oriented position angles of the material in the equatorial 'disc' are not matched by this model. Further modelling with multiple scattering for the central disc was not able to produce the observed pattern of radially oriented polarization vectors.

None of these alterations in geometry can simply explain the central finger and it seems most probable that it is indeed a distinct feature with a different tilt or composed of smaller grains. However the trend in polarization along the axis of this feature could more easily be attributed to a curve of the feature from close to the plane of the sky (i.e. towards the backside of the lobe) towards the line of sight, rather than a continuous change in grain properties. Given the fast outflow from the star (the CO data show a linear increase of radial velocity with deprojected distance of $8.9 \, \mathrm{km \, s^{-1} \, arcsec^{-1}}$, Alcolea et al. 2000) and its variability, an outflow with temporally varying dust properties could perhaps not be excluded. Polarimetry at different wavelengths for this feature could test if the grain properties differ from the surroundings. Clearly high spatial resolution spectra are required to measure radial velocities along this feature in order to distinguish a differing outflow direction. However this is not simple if the feature is only visible in scattered light since polarization velocity modelling is required (see Meaburn et al. 1993). Emission lines such as [N II] and [S II] from shocked gas would be a discriminating probe of the geometry of this feature. At present there is no evidence that this is a true jet until high spatial resolution imaging or spectrometry reveal intrinsic forbidden line emission.

The N lobe finger and the eastern loops in both lobes have such a remarkably high polarization which implies very stringent limitations to these features. They must be highly collimated otherwise the change in scattering angle across them would dilute the polarization; the dust must consist of very small particles so that only Rayleigh scattering is occurring with no admixture of large grains; there must be very little local emission from the grains or gas. The method to produce bipolar outflows is usually taken as interacting winds (e.g. Icke et al. 1989) or magnetic fields (Garcia-Segura et al. 1999). The presence of highly collimated dust, which is considered to have been ejected by the slow, dense wind in the Asymptotic Giant Branch (AGB) phase has not previously been explicitly considered in the hydrodynamic models. Since the central star of OH 231.8+4.2 is still too cool to ionize the nebula, the shaping of the dust features must have occurred by compression and/or erosion by the cool fast wind, which is deduced from the high molecular line outflow velocity (Alcolea et al. 2000). Alternatively the red giant wind is itself asymmetric and the collimated features arise in wind collimation at the star surface. Garcia-Segura et al. (1999) have shown that stellar magnetic fields of hundreds of Gauss together with stellar rotation rates close to critical rotation speed can produce highly collimated outflows from AGB and post-AGB stars. The very high polarization values, implying strong confinement, strongly suggest that magnetic fields or instabilities could play a part. The HST press release image of OH 231.8+4.2 (PRC 99-39) shows a series of undulations along the N finger and

the NE filament which present evidence of clumping that could arise from collimation of magnetic origin. If magnetic collimation does occur, then there may be microscopic alignment of grains, which could contribute to the very high linear polarization values observed, and would also produce measurable circular polarization. Such microscopic alignment of grains is also suggested for the equatorial disc on the basis of the large scale pattern of radially aligned polarization vectors. Mid-IR polarimetry would allow direct detection of polarized emission from aligned grains, as found for the Homunculus nebula around η Carinae (Aitken et al. 1995) for example.

4.3. New southern knot?

On the unrotated O and E ray images, there is a stellar (unresolved) knot on the projected major axis of the nebula at $36''$ offset from the position of QX Pup in the direction of the northern lobe. However on the $45°$ rotated images this knot is off the imaged area, so its polarization cannot be measured from these data. This could be a star but its position on the projection of the major axis of the nebula is suggestive. Although this is the lower velocity lobe (e.g. Alcolea et al. 1996), it may be a high velocity ejectum similar to the knots identified by Reipurth (1987) in the arc shaped nebula to the south of the southern lobe. Follow up emission line imaging and/or spectrometry are suggested to confirm its association with OH 231.8+4.2.

5. Conclusions

A linear polarization map of OH 0231.8+4.2 has been obtained in the K_S band with the SOFI multi-mode instrument. A wealth of structure is revealed in the polarization and two elongated features in the northern bipolar lobe have very high linear polarization. A geometrical model with bipolar lobes and an equatorial disc is proposed which accounts for some of these features. However the high polarization finger in the northern lobe, and the position angle of polarization vectors in the surrounding (disc) material, are not explained. Higher spatial resolution polarimetry of OH 231.8+4.2 is achievable from the ground with AO, and polarization maps at different wavelengths would help further understanding of this fascinating target.

References

Ageorges N., Walsh J. R., 1999, A&AS 138, 163

Aitken D.K., Smith C.H., Moore T.J.T., Roche P.F., 1995, MNRAS 273, 359

Alcolea J., Bujarrabal V., Contreras C.S., 1996, A&A 312, 560

Alcolea J., Bujarrabal V., Castro-Carrizo A., et al., 2000, In: Kastner J.H., Soker N., Rappaport S. (eds.) Asymmetrical Planetary Nebulae, ASP Conf. Ser. XXX (in press)

Bastien P., Ménard F., 1990, ApJ 364, 232

Cohen M., 1981, PASP 93, 288

Cohen M., Dopita M.A., Schwarz R.D., Tielens A.G.G.M., 1985, ApJ 297, 702

Devillard N., 1997, The Messenger 87, 19

Dougados C., Lena P., Ridgeway S., Chistou J., Probst R., 1991, In: Elstron R. (ed.) Astrophysics with IR Arrays, ASP Conf. Ser. 14, 152

Garcia-Segura G., Langer N., Różyczka M., et al., 1999, ApJ 517, 767

Heckert P.A., Zeilik M., 1983, MNRAS 202, 531

Hildebrand R.H., 1983, Q.J. Astro. Soc. 24, 267

Icke V., Preston H.L., Balick B., 1989, AJ 97, 462

Kastner J.H., Weintraub D.A., Zuckerman B., et al., 1992, ApJ 398, 552

Kastner, J. H., Weintraub, D. A., 1995, AJ 109, 1211

Kastner J.H., Weintraub D.A., Merrill K.M., Gatley I., 1998, AJ 116, 1412

Kobayashi Y., Kawara K., Maihara T., et al., 1978, PASJ 30, 377

Mathis J.S., 1990, ARA&A 28, 37

Meaburn J., Walsh J.R., Wolstencroft R.D., 1993, A&A 268, 283

Naghizadeh-Khouei J., Clarke D., 1993, A&A 274, 968

Reipurth B., 1987, Nat. 325, 787

Moorwood A., Cuby J.-G., Lidman C., 1998, The Messenger 91, p. 9

Scarrott S.M., Rolph C.D., Wolstencroft R.D., 1990, MNRAS 243, 462

Shure M., Sellgren K., Jones T.J., Klebe D., 1995, AJ 109, 721

Turner B.E., 1971, ApJ 73

Turnshek D.A., Bohlin R.C., Williamson R.L., et al., 1990, AJ 99, 1243

Wardle J.F.C., Kronberg P.P., 1974, ApJ 194, 249

Woodward C.E., Forrest W.J., Pipher J.L., Moneti A., Shure M.A., 1989, ApJ 337, 754